



Detailed comparative analysis of environmental microparticle deposition characteristics between human and monkey nasal cavities using a surface mapping technique

Yidan Shang ^{a,b}, Jingliang Dong ^{b,*}, Fajiang He ^a, Kiao Inthavong ^b, Lin Tian ^b, Jiyuan Tu ^b

^a College of Air Transportation, Shanghai University of Engineering Science, Shanghai 201620, China

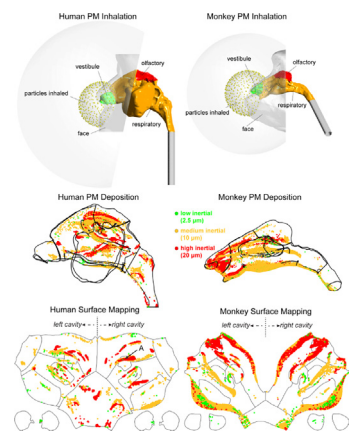
^b School of Engineering, RMIT University, PO Box 71, Bundoora, VIC 3083, Australia



HIGHLIGHTS

- A cross-species particulate matter (PM) exposure study in nasal airways was conducted.
- A novel surface mapping technique is utilized to identify deposition hot spots.
- PM profiles can be collapsed into a single equation as a function of Stokes number.
- Predominant PM deposition differences are observed in the vestibule and floor region.
- This study is expected to improve cross-species toxicological data extrapolation.

GRAPHICAL ABSTRACT



ARTICLE INFO

Editor: Pingqing Fu

Keywords:

Particulate matter
Inhalation toxicology
Cross-species extrapolation
Nasal cavity
Computational fluid dynamics
Surface mapping

ABSTRACT

Inhaled particulate matter is associated with nasal diseases such as allergic rhinitis, rhinosinusitis and neural disorders. Its health risks on humans are usually evaluated by measurements on monkeys as they share close phylogenetic relationship. However, the reliability of cross-species toxicological extrapolation is in doubt due to physiological and anatomical variations, which greatly undermine the reliability of these expensive human surrogate models. This study numerically investigated in-depth microparticle transport and deposition characteristics on human and monkey (*Macaca fuscata*) nasal cavities that were reconstructed from CT-images. Deposition characteristics of 1–30 μ m particles were investigated under resting and active breathing conditions. Similar trends were observed for total deposition efficiencies and a single correlation using Stokes Number was fitted for both species and both breathing conditions, which is convenient for monkey-human extrapolation. Regional deposition patterns were carefully compared using the surface mapping technique. Deposition patterns of low, medium and high inertial particles, classified based on their total deposition efficiencies, were further analyzed in the 3D view and the mapped 2D view, which allows locating particle depositions on specific nasal regions. According to the particle intensity contours and regional deposition profiles, the major differences were observed at the vestibule and the floor of the nasal cavity, where higher deposition intensities of medium and high inertial particles were shown in the monkey case than the human case. Comparisons of airflow streamlines indicated that the cross-species variations of microparticle deposition patterns are mainly contributed by two factors. First, the more oblique directions of monkey nostrils result in a sharper airflow turn in the

* Corresponding author.

E-mail address: jingliang.dong@rmit.edu.au (J. Dong).

vestibule region. Second, the monkey's relatively narrower nasal valves lead to higher impaction of medium and high inertial particles on the nasal cavity floor. The methods and findings in this study would contribute to an improved cross-species toxicological extrapolation between human and monkey nasal cavities.

1. Introduction

Particulate matter (PM) is the dominant component of ambient air pollution that causes 7 million premature deaths worldwide per year, with a high risk in low- and middle-income countries (World-Health-Organisation, 2021a). The filtering function of the nasal cavity makes it a frontline defender to the respiratory system and a major site for exposure toxicological assessment. The nasal cavity is vulnerable to environmental toxic agents due to the abundant vascular plexus beneath the respiratory epithelium. The levels of PM₁₀ and PM_{2.5} are highly associated with allergic rhinitis and rhinosinusitis as they irritate nasal mucosa and disrupt epithelial barrier functions (World-Health-Organisation, 2021b; Health-Effects-Institute, 2020; Mo, 2019). Also, emerging studies raised concerns that the olfactory region may provide a pathway for the inhaled particles to enter the central neural system and cause neural disorders (Doty, 2008; Attems et al., 2014; Shang et al., 2021).

Due to ethical restrictions, toxicological tests of environmental PM exposure have been routinely conducted on monkeys (non-human primates, NHPs) to evaluate human's physiological responses to inhaled PM (Phillips et al., 2014). Compared to rodents such as rats, mice, hamsters and guinea pigs, monkeys possess high level of biological similarities to humans due to their close phylogenetic relationship. This is also the case in the nasal structures that filter inhaled particles (Phillips et al., 2014; DeSesso, 1993). However, due to cross-species physiological and anatomical variations, the reliability of toxicological extrapolation from monkey to human nasal cavity is in doubt as the in-depth knowledge of cross-species comparative regional particle dose is lacking (Schroeter et al., 2008; Corley et al., 2012; Corley et al., 2021). Besides, in response to the ongoing supply shortage of laboratory monkeys in the wake of COVID-19 vaccine and treatment development, international efforts are underway to reduce and replace the use of animals in in-vivo toxicity studies with in-vitro studies and numerical modelling (Corley et al., 2021; Subbaraman, 2021; EPA, 2018). There is a pressing need to evaluate comparative physiological response to inhaled microparticles between monkey and human nasal cavities. To achieve this goal, development of computational approaches based on virtual inhalation exposure studies using the existing human medical images and the monkey digital databases is essential for modelling monkey-human equivalent exposures standards and toxicological dosimetry extrapolation of environmental pollutants. Monkey medical images are readily available in the Kyoto University Primary Research Institute (KUPRI) (KUPRI, 2022), which have collected a database of monkey CT and MRI scans to provide new insights into primate and mammalian evolution.

Previous in-vivo measurements using radioactive imaging techniques revealed information of microparticle deposition sites in the monkey respiratory airways (baboons (Albuquerque-Silva et al., 2014) and rhesus macaques (Dabisch et al., 2017)) and found the deposition distributions in thoracic and extrathoracic regions were comparable to the human case (Albuquerque-Silva et al., 2014). Although there are very limited in-vivo measurements conducted in monkey and human nasal, a few in-vitro experimental investigations were conducted on respiratory airway replicas to examine the microparticle inhalation deposition characteristics in human and monkey nasal cavities. In these in-vitro studies, measurements of microparticle (0.5–10 µm) deposition efficiencies also showed considerable similarities in rhesus monkey and human nasal replicas (Kelly et al., 2005; Kesavan et al., 2020). Equivalent Stokes Number (Stk), a scale factor based on minimum cross-sectional area of the nasal cavity, was used to normalize

microparticle total deposition efficiencies among monkey subjects with individual variations.

In recent years, numerical simulations have been conducted to collect detailed region-specific particle deposition features. Monkey and rodent respiratory models were adopted to conduct numerical studies in Kimbell et al. (Kimbell, 2006) and Corley et al. (Corley et al., 2012), where comparative gaseous dosimetry were assessed and compared among human, rats and monkeys. These studies found higher similarities between humans and monkeys than human and rats. Our previous works numerically investigated the intricate interplay between nasal anatomy, airflow dynamics and diffusive nanoparticle deposition patterns (Dong et al., 2021a; Lu Phuong et al., 2018; Tian et al., 2022; Vahaji et al., 2022). Converting gas to nanoparticles, Dong et al. (Dong et al., 2021a) used discrete phase method (DPM) to investigate regional particle deposition in an infant cynomolgus monkey nasal cavity and found the middle and lower portions were preferred sites for uptake of diffusive nanoparticles. Comparative airflow characteristics have been extensively visualized and analyzed. Regarding microparticle deposition in nasal cavities, numerical simulations have been conducted to collect comparative deposition characteristics in human (Shi et al., 2007; Schroeter et al., 2011; Dong et al., 2019; Inthavong, 2020) and monkey (Lu Phuong et al., 2018; Schroeter et al., 2013; Geisler et al., 2019) nasal cavities. Although many in-silico studies using monkey and human airways have been conducted in literature, the majority of them were focused on either the inhalation exposure to gaseous substances or the diffusive nano-sized particles. There is a lack of studies about the transport and deposition analysis of inhalation exposure to microparticles with inertia dominated particle transport behavior. To the best of our knowledge, only a single study exists, by Lu Phuong et al. (Lu Phuong et al., 2018), that explored cross-species comparative region-specific deposition for microparticles. This study investigated the deposition of 1–10 µm particles and found that the normalization of Stk and minimal cross-sectional area A_{min} are appropriate for cross-species microparticle total deposition extrapolations. The regional depositions in vestibule, central passage and nasopharynx showed considerable differences due to apparent cross-species geometrical variations. There were several limitations in this pioneer research. First, the simulations were based on simplified nasal models without including maxillary sinus. Second, the nasal models were partitioned to regions based on major anatomical regions (vestibule, central passage and nasopharynx) and this was not enough to accurately locate particle deposition locations in the highly folded main passage walls.

Due to the limitation of available visualization method and appropriate analysis tools, it remains unclear how the cross-species airflow features caused by variability in nasal geometry can be related to the human and monkey regional deposition characteristic, especially in the main passage that hosts the olfactory region and spiral turbinate structures. To address this research gap, this study numerically investigated qualitative and quantitative microparticle deposition characteristics in nasal subjects of a human and a *Macaca fuscata* monkey. Comparative region-specific microparticle deposition analysis was focused on four major nasal regions with interests: vestibule, olfactory, maxillary sinus and main passages. The main passages were further partitioned into septum, middle meatus, inferior meatus, lateral wall and nasopharynx. A surface mapping method (Inthavong et al., 2014; Shang and Inthavong, 2019) was applied to reveal high-fidelity region-specific microparticle deposition patterns. Lastly, coupled with comparative nasal airflow features, this study further analyzed the mechanisms behind the cross-species microparticle deposition variations caused by major geometrical features.

2. Methods

2.1. Nasal geometry

The human nasal model was reconstructed from a high-resolution CT scan of a healthy 21-year-old Asian male with image dimensions 512×512 , pixel spacing 0.45 mm and slice thickness 0.5 mm. The CT dataset was acquired by a Dual Source CT scanner (Siemens Healthineers, Erlangen, Germany) in Xi'an, Shaanxi Province of China. The data collection was approved by the Human Research Ethics Committee at the Second Affiliated Hospital of Xi'an Jiaotong University. The monkey nasal model was reconstructed from a micro-CT scan of a healthy 9-year-old female Japanese macaque (*Macaca fuscata*, 8.7 kg), with image dimensions 512×512 , pixel spacing 0.263 mm and slice thickness 0.5 mm. The monkey CT dataset was from an open database Digital Morphology Museum KUPRI (KUPRI, 2022), Japan, labeled as PRICL No.46.

Identical components of both nasal models (Fig. 1a and b) including nasal passages, olfactory regions, maxillary sinus, nasopharynx and faces were segmented in a medical imaging segmentation software 3D-Slicer (version 4.11) and were cleaned in a geometry processing software Geomagic Wrap (version 2021). A hemisphere was attached in front of each face to mimic the external environment with realistic inflow near nostrils and to provide a domain for realistic microparticle releasing method. The nasopharynx of the monkey model was further extended to larynx and trachea to have direct comparisons with experimental measurements. Straight pipes were attached to outlets of both models to ensure realistic outflow boundary conditions. Each nasal model was partitioned into three epithelial regions, including vestibule region (covered with squamous epithelium, colored in green), olfactory region (covered with olfactory epithelium, colored in red) and respiratory region (covered with respiratory epithelium, colored in yellow). To minimize the effects of breathing zone airflow (~ 2.34 cm from the nostril (Shang et al., 2015)) on released

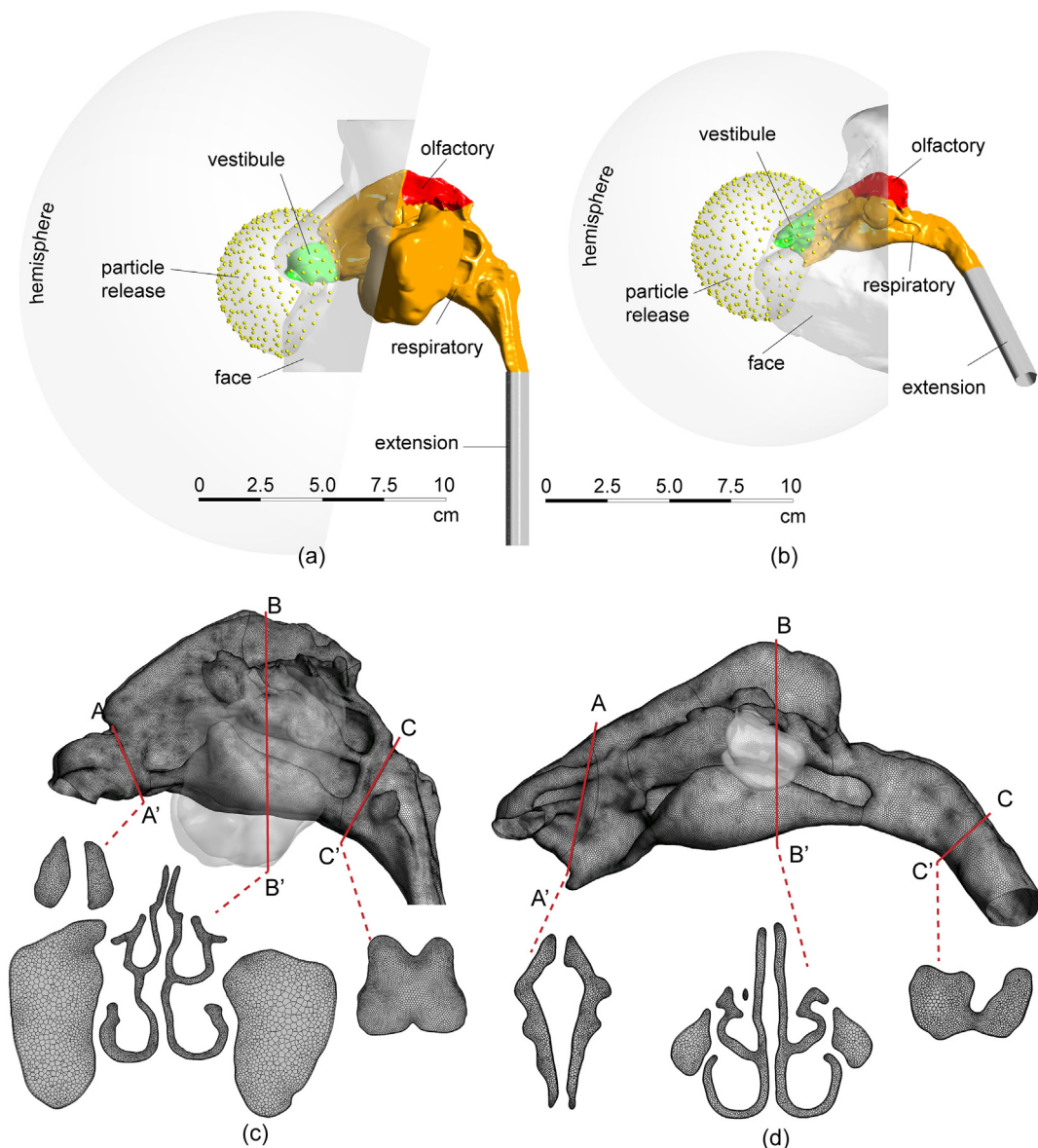


Fig. 1. Geometrical nasal models of (a) human and (b) monkey. Maxillary sinuses were retained for both models. Nasal walls of both models were partitioned into vestibule (green), olfactory (red) and respiratory passages (orange). The faces and breathing zones were included to ensure realistic inflow characteristics near nostrils. Particles were evenly released on spheres around breathing zones. Nasal models were discretized with polyhedral meshes for (c) human and (d) monkey. Five prism layers were generated to capture near-boundary airflow and particle features. Three cross sections, including nasal valve (AA'), center of main cavity (BB') and choana (CC'), are highlighted to reveal the detailed volume mesh elements.

particles, a sphere with radius of 3 cm centered at the tip of nostrils was created in front of each face as the source of microparticle releasing.

The computational domains were discretized by polyhedral mesh elements, and then refined in regions with high curvature and small gaps using Ansys Fluent Meshing (version 2022R1). Surface meshes and mesh elements of three cross-sections located at the nasal valve, the middle of nasal passages and choana are presented in Fig. 1c and d. High level of symmetry is shown on the monkey nasal cavity, but the nasopharynx geometry is slightly biased. Whereas for the human model, asymmetric geometry can be found in the nasal cavity due to septum deviation. Three prism layers, with first layer aspect ratio of 8 and growth rate of 1.2, were attached to nasal walls to accurately capture near-boundary airflow features. A mesh independence test was performed for each species under three refinements (coarse, medium and fine) and the optimal mesh (medium) with 2.92 million cells and 2.31 million cells were selected for the human and monkey cases. The maximum skewness of selected meshes was 0.6. Comparing with 1.5–3.8 million meshes used in our previous studies regarding human and monkey nasal models (Dong et al., 2021a; Tian et al., 2022; Vahaji et al., 2022), the number of mesh elements in this study is within a reasonable range.

2.2. Governing equations and boundary conditions

The airflow was solved by the 3D steady incompressible Navier-Stokes governing equations,

$$\nabla \cdot \vec{v} = 0 \quad (1)$$

$$(\vec{v} \cdot \nabla) \vec{v} = -\frac{\nabla p}{\rho_{air}} + \frac{\mu}{\rho_{air}} \nabla^2 \vec{v} \quad (2)$$

where \vec{v} is the air velocity vector, p is the static air pressure, ρ_{air} is the air density and μ is the air viscosity. The simulation was conducted in Ansys Fluent (version 2022R1). The $k - \omega$ SST model was used to model the turbulence of nasal airflow and the SIMPLE algorithm was adopted for pressure-velocity coupling. The heat exchange is usually introduced to simulations when analysing the nasal air-conditioning function, particle hygroscopic growth and particle evaporation (Vahaji et al., 2022; Ma et al., 2018; Siu et al., 2021). However, this study focuses on investigating aerosol particle transport characteristics with specific particle sizes. For simplicity, particle hygroscopic growth and evaporation processes were not considered. The energy equation and heat exchange were therefore not included in the simulations. The simulations were considered converged when all residuals reached 10^{-6} .

Microparticles were tracked with discrete phase model (DPM) under Lagrangian framework,

$$\frac{d\vec{v}_p}{dt} = \vec{f}_D + \vec{g} \quad (3)$$

\vec{v}_p is the velocity of a microparticle, \vec{g} is the gravity acceleration and \vec{f}_D is the drag force per unit mass,

$$\vec{f}_D = \frac{18\mu}{d_p^2 \rho_p} \frac{C_D Re_p}{24} \left(\vec{v}_{air} - \vec{v}_p \right) \quad (4)$$

where d_p and ρ_p are size and density of a microparticle. Re_p and C_D are particle Reynolds number and drag coefficient,

$$Re_p = \frac{\rho_p d_p}{\mu} \left| \vec{v}_{air} - \vec{v}_p \right| \quad (5)$$

$$C_D = a_1 + \frac{a_2}{Re_p} + \frac{a_3}{Re_p^2} \quad (6)$$

a_1 , a_2 and a_3 are empirical parameters (Morsi and Alexander, 1972). The 6th-order Runge-Kutta scheme was used for particle tracking.

Power law (allometric) equations have been widely adopted to depict the relationship between animal body weight (BW, unit kg) and respiratory minute volume (V_m , unit L/min). Bide et al. (Bide et al., 2000) collected data of 2616 animals and 18 species from mice to horses and statistically developed an allometric respiration equation for non-anaesthetized (active) animals,

$$V_m = 0.499 BW^{0.809} \quad (7)$$

Calculating from eq. (7), the respiratory minute volume flow rate for an 8.7 kg active monkey is 2.87 L/min. The equivalent steady inspiratory flow rate under active condition was set as 5.74 L/min considering the ratio between inhalation phase and exhalation phase was approximately 1 for monkey (MacLoughlin et al., 2016). Accordingly, the inspiratory flow rate for the monkey under resting condition was half of that in the active condition, namely 2.87 L/min. These airflow rates were also adopted from our previous study (Vahaji et al., 2022). Similarly, for a typical 70 kg male human, the inspiration flow rates for the resting and active conditions were calculated 15 L/min and 30 L/min, respectively, which was also widely adopted by existing studies (Shang and Inthavong, 2019; Dong et al., 2017).

The hemisphere in front of faces were set pressure inlets (0 Pa), mimicking environmental breathing conditions and realistic airflow profiles near nostrils. The outlet boundaries at the exits of extension pipes were set velocity outlets, drawing air from nasal cavities. All the rest boundaries were set no-slip walls. For each case, 100,000 particles were evenly released at a hemisphere with zero initial velocity. The DPM condition at the nasal walls was set to “trap”, where the Lagrangian particle tracking is terminated when individual particle hits the nasal walls. The rest of the boundaries were set to “escape”. The deposition efficiency was defined as the number ratio of the deposited microparticles to the inhaled microparticles.

The particle Stk, reflecting geometry-related particle inertial characteristics, were calculated to normalize microparticle total deposition efficiencies between species and among variant inspiration airflow rates. The Stk is defined as,

$$Stk = \frac{\rho_p d_p^2 u_c}{18\mu_{air} d_c} = \frac{2\rho_p d_p^2 Q}{9\pi\mu_{air} d_c^3} \quad (8)$$

where Q is inspiration flow rate, $u_c = 4Q/(\pi d_c^2)$ is the equivalent characteristic air velocity and d_c is the characteristic dimension of the nasal passage. The calculation of the Stokes number largely depends on the equivalent characteristic diameter that is determined by the nasal geometry. To simplify the calculation, in this study, the d_c was estimated by the average equivalent characteristic diameter of nostrils as listed in Table 1.

Table 1
Average nostril diameters for calculating stokes numbers.

	Left nostril			Right nostril			Average Diameter (mm)
	Area (mm ²)	Perimeter (mm)	Diameter (mm)	Area (mm ²)	Perimeter (mm)	Diameter (mm)	
Human	94.9	35.9	10.6	99.3	37.4	10.6	10.6
Monkey	35.5	24.5	5.80	36.8	25.1	5.86	5.83

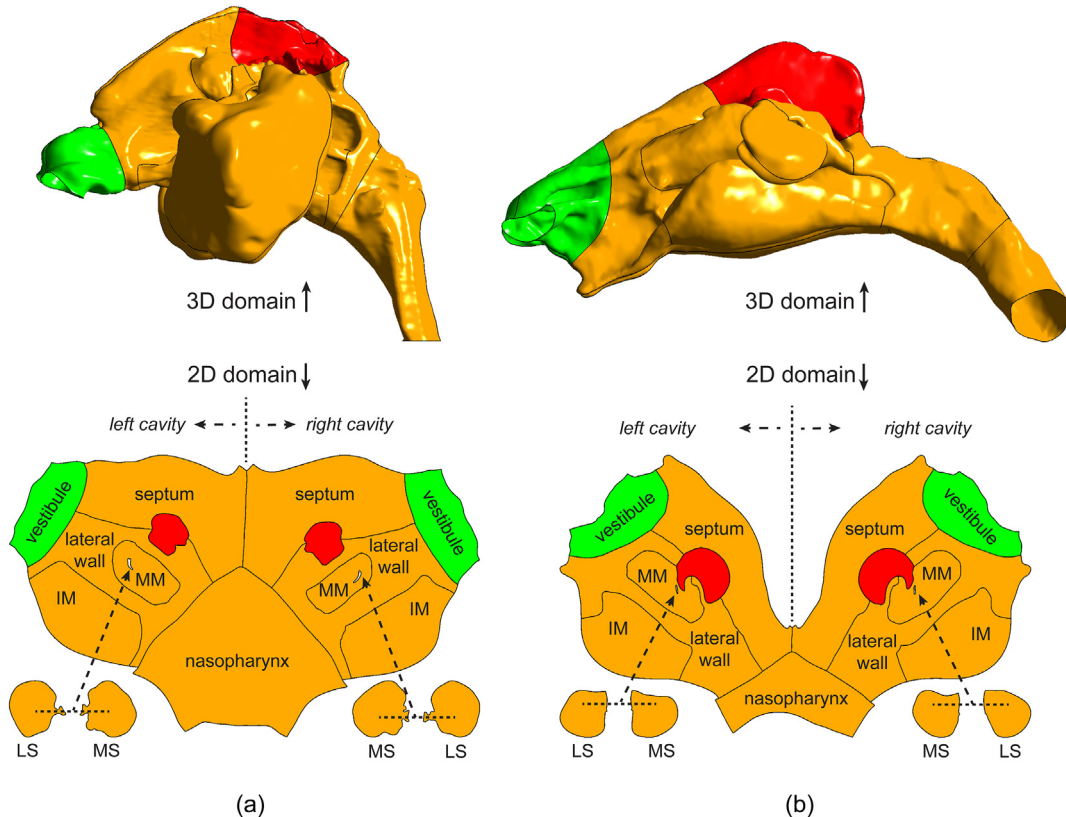


Fig. 2. Surface mapping strategies for (a) human and (b) monkey. The nasal cavity models were cut at the floor and then unwrapped from the 3D domain into the 2D domain. Maxillary sinuses were mapped separately and scaled properly. The respiratory passages were further partitioned into several anatomical regions, including septum, nasopharynx, lateral wall, middle meatus (MM), inferior meatus (IM), lateral maxillary sinus (LS) and medial maxillary sinus (MS).

2.3. Anatomical division and surface mapping

To allow direct comparisons of particle deposition patterns across the entire nasal cavity surface for human and monkey cases, the surface mapping technique was used to transform the 3D surface boundaries onto a flat 2D domain, retaining connections between anatomical nasal regions. The regions covered with respiratory epithelium (colored in yellow in Fig. 2) were separated into sub-regions including septum, middle meatus (MM), inferior meatus (IM), lateral walls, nasopharynx and maxillary sinus, to conveniently locate microparticle deposition on 2D domains. The maxillary sinus region was further separated into lateral part (LS) and medial part (MS), and their connections to the ostium on nasal passages were indicated by dashed lines and arrows as shown in mapped views in

Fig. 2. The maxillary sinus regions in 2D domains were significantly scaled to fit into a normalized mapping layout, without reflecting actual surface areas in original 3D domains.

3. Results

3.1. Nasal cavity measurements and comparison

To quantify cross-species shape variations, measurements of the major anatomical nasal regions are compared between human and monkey models in Table 2. Although the total surface area (excluding maxillary sinus and nasopharynx) of human nasal cavity is around twice of that monkey nasal cavity, similar area percentage distributions are found between

Table 2
Geometrical comparison of major anatomical regions for human and monkey nasal models.

Region name	Human nasal model		Monkey nasal model	
	Area (cm ²)	Percentage nasal cavity (%)	Area (cm ²)	Percentage nasal cavity (%)
Vestibule	14.7 (12.6 ^a)	7.4 (6.2 ^a , 8.2 ^b)	9.9 (9.0 ^a)	9.1 (11.8 ^a , 12 ^c)
Olfactory	17.2	8.6 (2.8–10.9 ^d)	13.4	12.3 (14 ^e)
Septum	38.8	20.5	22.8	20.9
Lateral wall	55.7	29.4	24.7	22.7
Inferior meatus	35.3	18.6	19.5	17.9
Middle meatus	27.9	14.7	18.6	17.1
Nasal cavity total	199.6 (201.6 ^a)	100.0	108.9 (75.7 ^a)	100.0
Maxillary Sinus	104.6		6.8	
Nasopharynx	27.9		6.6	

^a Schroeter et al. (2014) (Schroeter et al., 2014).

^b Schroeter et al. (2008) (Schroeter et al., 2008).

^c Gross et al. (1987) (Gross et al., 1987).

^d Illum et al. (2004) (Illum, 2004) and Garcia et al. (2015) (Garcia et al., 2015).

two species. Within the nasal cavity, the largest surface area coverage are the lateral nasal wall (29.4 % and 22.7 % for human and monkey) and the septum (20.5 % and 20.9 % for human and monkey), followed by inferior meatus (18.6 % and 17.9 % for human and monkey) and middle meatus (14.7 % and 17.1 % for human and monkey). The olfactory surface areas occupy 8.6 % and 12.3 % of the nasal cavity in human and monkey respectively, indicating slightly higher olfactory sensitivity for the monkey. Comparisons with available data from literature are presented for the vestibule regions, olfactory regions and total nasal cavity surface area. The area percentage of the human and monkey vestibule regions are 7.4 % and 9.1 %, respectively, and they are both within the range measured in literature. The definition of the borders of human olfactory epithelium has been controversial. Illum et al. (Illum, 2004) and Garcia et al. (Garcia et al., 2015) collected multiple human nasal models and estimated the olfactory area percentages to be 3.0 %, 2.8 %, 5.5 % and 10.9 %. The area percentage of human olfactory region in this study is 8.6 %, which is also within the range in literature. The measurement of the area percentage of monkey olfactory region is rare in literature. Gross et al. (Gross et al., 1987) estimated the area percentage of 14 %, which is slightly higher than that in this study. However, considering individual variations, surface areas and percentages are still within reasonable ranges for all anatomical regions.

3.2. DPM model validation and cross-species deposition correlation

To validate the numerical model, microparticle deposition efficiencies (DE) in the nasal cavity against impaction parameter (IP) are compared with literature data for both human and monkey cases, as seen in Fig. 3a and b. The DE is defined as the ratio of the number of particles deposited to the number of particles inhaled through nostrils. The impaction parameter ($IP = d^2Q$), representing the inertial impact of inhaled microparticle, is the combination of particle size d and inspiratory flow rate Q , and the units are normalized to $\mu\text{m}^2 \cdot \text{cm}^3/\text{s}$.

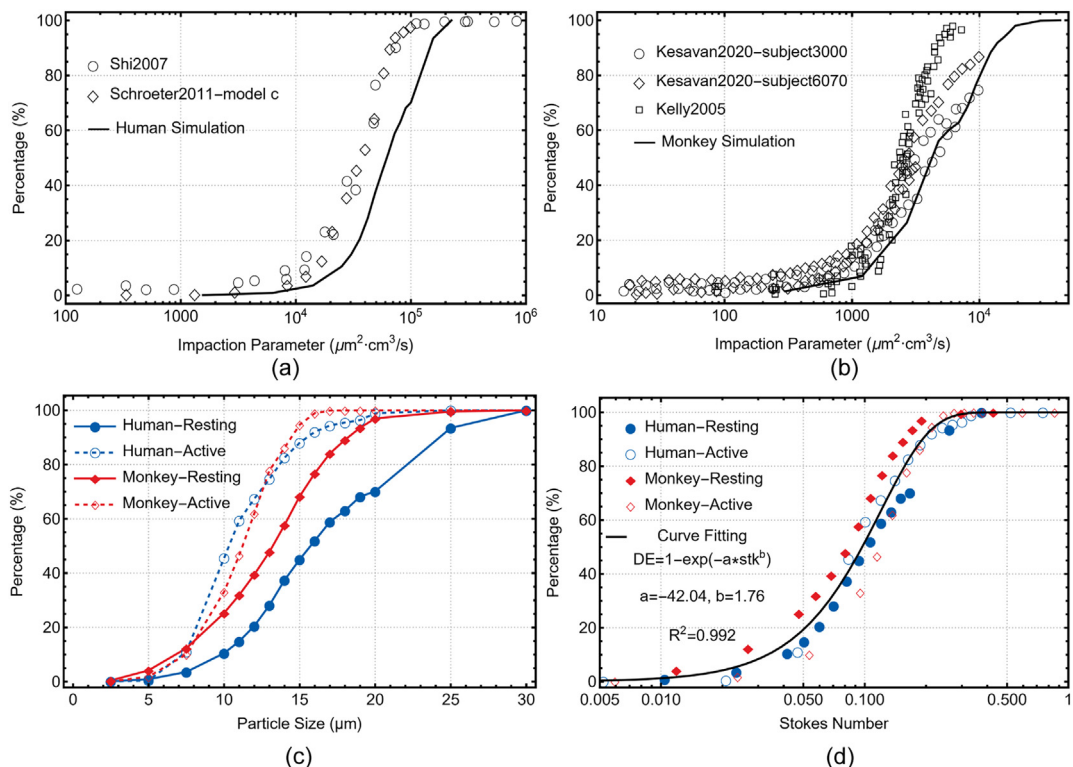


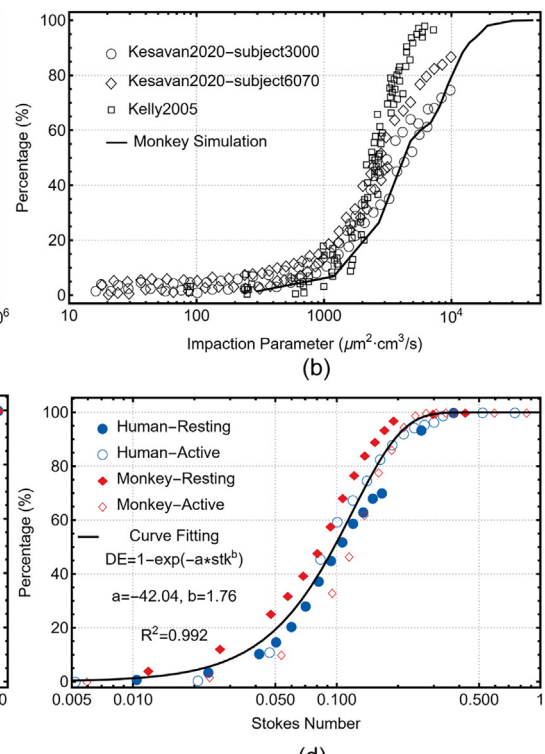
Fig. 3. Deposition efficiency data plotted against impaction parameters for (a) human and (b) monkey. Simulated results were compared with existing literature for validation. Deposition efficiency data were plotted against (c) Particle Size and (d) Stokes Number (Stk) for human and monkey cases under resting and active breathing conditions. Circle and diamond symbols represent simulated results from this study. The simulated results were normalized into a single correlation using Stk. The black solid curve in (d) illustrates the fitted correlation, with parameters ($a = -42.04$, $b = 1.76$) as listed in (d).

For the human case, although the simulated DE results are relatively lower than those in literature of Shi et al. (Shi et al., 2007) and Schroeter et al. (Schroeter et al., 2011), they are within an acceptable range considering individual variation and biological heterogeneity. More importantly, the current DE results present a S-shape profile, indicating a similar trend with results in literature. For the monkey case, the nasal cavity geometry model was extended to larynx to match the respiratory components for DE calculation in literature. DE measurements of three monkey respiratory models from Kesavan et al. (Kesavan et al., 2020) and Kelly et al. (Kelly et al., 2005) were compared with current simulation results for monkey microparticle DE validation. Subject 3000 and subject 6070 were selected from Kesavan et al. (Kesavan et al., 2020) as they share similar age and body weight with the monkey subject in this study. The DE comparisons show that the simulation results are lower than that from Kelly et al. (Kelly et al., 2005) and the subject 6070 of Kesavan et al. (Kesavan et al., 2020) but matches the subject 3000 well. Overall, the simulation results of both human and monkey cases show good agreement with literature.

Fig. 3c demonstrates the DE versus particle size for human and monkey cases under resting and active conditions. The simulated data points plotted in circle and diamond symbols are connected with solid lines to illustrate particle deposition trends. In general, four curve profiles share the similar S-shape trend, in which the DE firstly stables at a low value and then sharply increases until reaching 100 %. Specifically, the curve profiles increase more rapidly in active conditions than resting conditions for both species. Four curve profiles merge into a single profile after converting particle sizes to Stk, as shown in Fig. 3d. The best correlation (with $R^2 = 0.992$) to depict the normalized profile was fitted as below,

$$DE = 1 - \exp(-42.04 \cdot Stk^{1.76}) \quad (9)$$

Similar trend was found in the normalized cross-species DE-Stk curve profile from Phuong et al. (Lu Phuong et al., 2018), confirming the reliability of the DE normalization method. For the monkey case, the range of Stk is



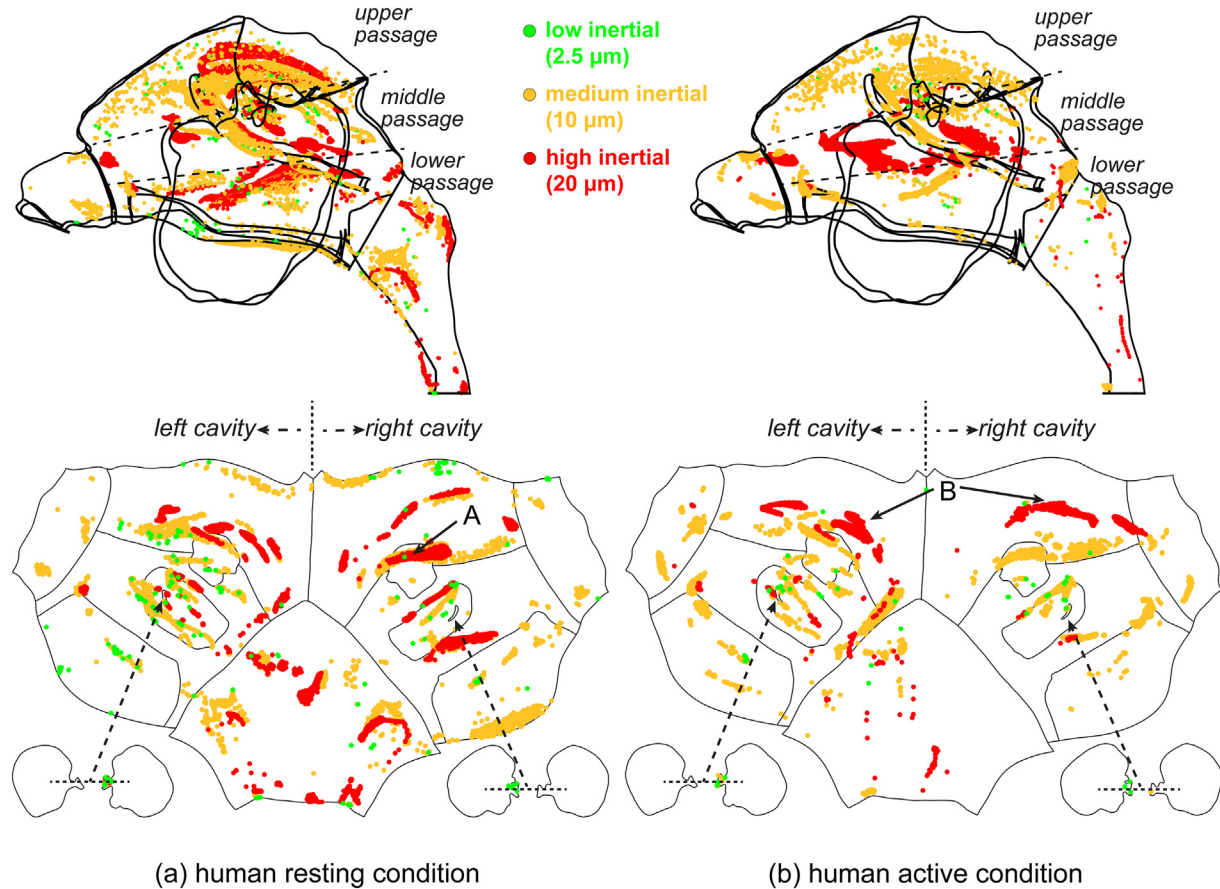


Fig. 4. Microparticle deposition locations on human nasal cavity walls under (a) resting and (b) active breathing conditions. 2.5 μm , 10 μm and 20 μm particles were selected to represent low, medium and high inertial particles.

one magnitude higher than that in Kesavan et al. (Kesavan et al., 2020). This is mainly due to the difference in the definition of Stk, as the average equivalent diameter of nostrils were selected for characteristic length in this study, as listed in Table 1, whereas the minimum cross-sectional areas were selected by Kesavan et al. (Kesavan et al., 2020). The fitted correlation confirms that the nostril features, which are proportional to the nasal scale and easier to measure, are also suitable for Stk calculations and cross-species microparticle deposition normalizations between human and monkey nasal geometries.

3.3. Comparisons of microparticle deposition patterns

As shown in Fig. 3c, the DE ranges for 2.5 μm , 10 μm and 20 μm are <5%, 10 % – 50% and >70%, respectively, for both human and monkey cases. These three particle sizes, selected as typical low, medium and high inertial particles, are suitable for visualizing particle deposition patterns characteristics. Fig. 4 shows their deposition patterns in the human nasal cavity wall under resting and active breathing conditions, as colored in green, yellow and red for low, medium and high inertial particles.

In general, for each breathing condition, low inertial particles are relatively more evenly distributed on the nasal cavity wall, whereas high inertial particles are more concentrated on specific ‘hot-spots’. Comparing between breathing conditions, particles are relatively more evenly distributed in the resting condition than in the active condition. For each particle type, a few particles enter the maxillary, depositing close to the ostium that are connected to the nasal passages. Specifically, the number of deposited low inertial particles is much less than medium and high inertial particles, and no deposition is found on the vestibule region. High inertial particles deposit on the whole nasal cavity wall except the inferior meatus. Interestingly, only a few high inertial particles deposit on vestibule in the active

breathing condition. Medium inertial particles deposit on all regions, and interestingly, apparent deposition on the vestibule region is for medium inertial particles only.

Different inhalation conditions do not lead to major changes for low and medium inertial particle deposition patterns, but have significant effects on high inertial particle deposition. In general, in the 3D view of the resting condition (Fig. 4a), high inertial particles reach the whole nasal cavity posterior to the vestibule, including upper, middle and lower passages and nasopharynx. The upper passage deposition is concentrated on the olfactory region of the right nasal chamber due to asymmetric nasal geometry, as seen in the label A in the mapped view. The middle and lower passage deposition is concentrated on the septum, the middle meatus and the lateral wall, respectively. On the contrary, in the active breathing condition (Fig. 4b), high inertial particles dominantly deposit on the septum region of the middle nasal passage, as seen in the label B.

Fig. 5 shows low, medium and high inertial particle deposition patterns in the monkey nasal cavity wall under resting and active breathing conditions. In general, similar to the human case, for each breathing condition, low inertial particles are relatively evenly distributed around the nasal cavity. Besides, only low inertial particles enter the maxillary sinus. Medium and high inertial particles present similar belt-shaped deposition areas on the nasal cavity wall. Their deposition on the maxillary sinus is not observed. Comparing between breathing conditions, particles in the resting condition reach more regions of the nasal cavity than in the active condition.

The airflow variations between two breathing conditions have observable effects on deposition patterns of all three particle types. The airflow in the active breathing condition prevents low inertial particles from depositing on the floor of the nasal cavity and prevents medium inertial particles from reaching the lateral wall and middle meatus. High inertial particles

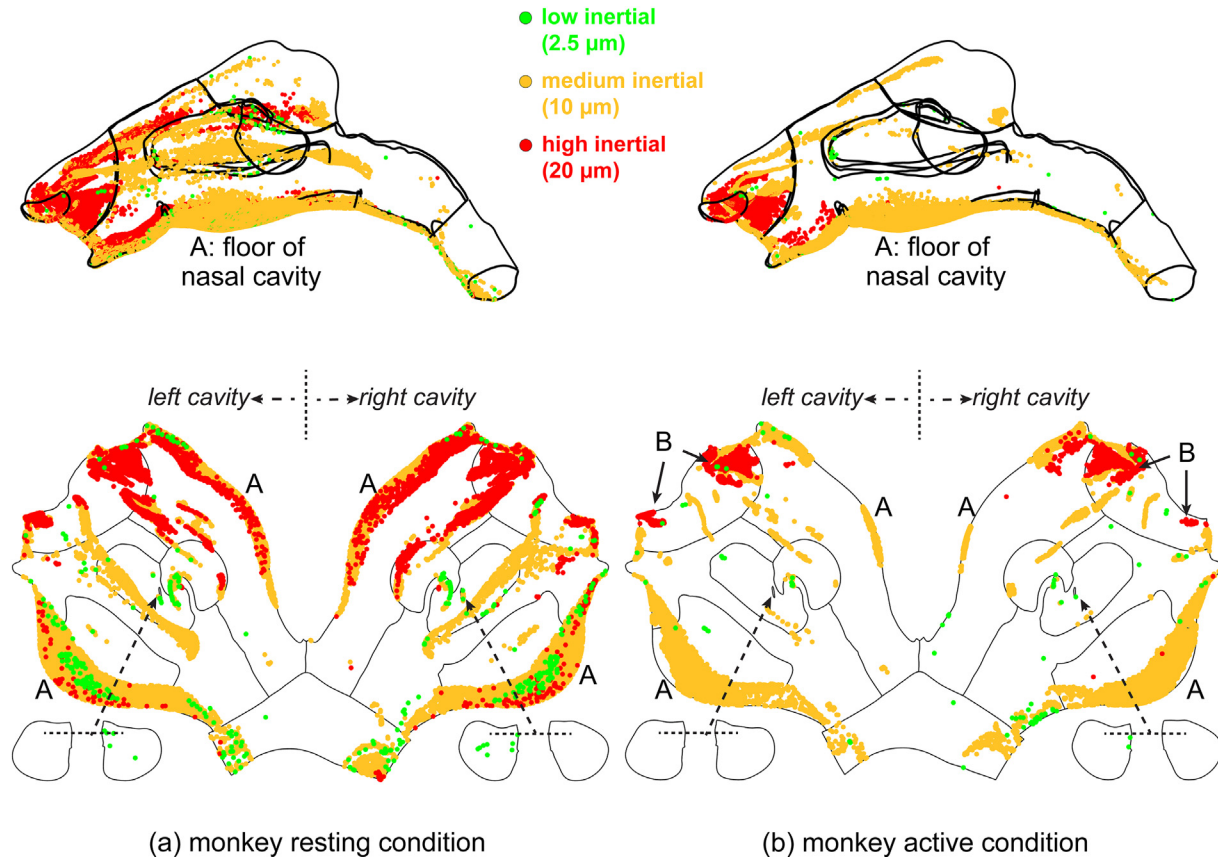


Fig. 5. Microparticle deposition locations on monkey nasal cavity walls under (a) resting and (b) active breathing conditions. 2.5 μm , 10 μm and 20 μm particles were selected to represent low, medium and high inertial particles.

deposit on the several nasal regions including vestibule, septum, floor of nasal cavity (label A) and olfactory regions in the resting condition, whereas their deposition locations are dominantly restricted on the vestibule region in the active condition, as seen in the label B.

To demonstrate accumulated deposited particles on the nasal cavity wall, comparisons of particle intensity (PI) contours between human and monkey are visualized in the mapped domains as shown in Figs. 6. The PI is defined as,

$$\text{PI} = \frac{\Delta N_p}{N_i \Delta S} \times 100\% \quad (10)$$

where ΔN_p is the number of deposited particles within a small control area surrounding a point of interest, ΔS is the corresponding surface area and N_i is the total number of inhaled particles. The unit of PI is 'DE per mm²' and the sampling radius is 0.5 mm, according to the optimal value in Dong et al. (Dong et al., 2021b). To reveal high PI spots, the upper limit of the PI value was truncated at 1 %/mm² and the PI lower than 0.001 %/mm² was not visualized.

In general, similar PI patterns are found for resting and active breathing conditions for both human and monkey cases. Low PI values (<0.01 %/m²) are observed for low inertial particles. As particles turn to medium inertial, the deposition coverage over the nasal cavity wall increases and several PI hotspots are observed. As particle inertial further increase to high inertial, the deposition coverage area shrinks, and PI hotspots are concentrated on a few locations.

For medium inertial particles, PI hotspots are found on two major locations for the human case, including the vestibule of the right cavity and the lateral walls of both cavities. As a comparison, two medium inertial particle PI hotspots for the monkey case are located at the vestibule and the belt-shaped areas are located at the floor of the nasal cavity (Fig. 6). For high

inertial particles, all PI hotspots on the human nasal cavity are dominantly shifted to the septum region. Similar phenomena are observed in the monkey case, as PI hotspots are mostly restricted in the vestibule region. Two major differences can be observed when comparing between two breathing conditions. In the human case, an additional hotspot is found in the left chamber, around the common border among septum, lateral wall and nasopharynx in the active breathing condition. In the resting breathing monkey case, there is a considerable belt-shaped high PI area stretching from the vestibule, extending to the lateral wall and covering part of the middle meatus. However, this hotspot disappears as the breathing condition turns to active.

Regional particle deposition efficiencies versus particle size are demonstrated in Fig. 7. Four regions, including vestibule, olfactory, maxillary sinus and the posterior-vestibule, were selected for plotting. The posterior-vestibule region represents the rest of the nasal cavity excluding vestibule, olfactory and maxillary sinus regions. In general, for both human and monkey cases, both resting and active breathing conditions result in a similar DE trend in all regions except the maxillary sinus region. The DE profiles, especially the high DE portions, are simply shifted to smaller particle size for the active breathing condition from larger size for the resting condition. This phenomenon is typical in the olfactory region, where DE profiles firstly increase, and then peak at 2.7 % (12 μm for active) and 3.3 % (17 μm for resting) for the human case and at 1.3 % (13 μm for active) and 2.8 % (17 μm for resting) for the monkey case. After that, the DE profiles gradually decrease to zero. Interestingly, human with resting breathing condition is the only scenario that considerable particles enter maxillary sinus, peaking at 0.36 % when the particle size reaches 16 μm .

Comparing human and monkey cases, the most significant difference of DE trends is observed in the vestibule region. In the monkey case, a S-shape profile is presented, which means almost all particles are trapped in the vestibule when the particle size reaches a certain value (18 μm and 25 μm

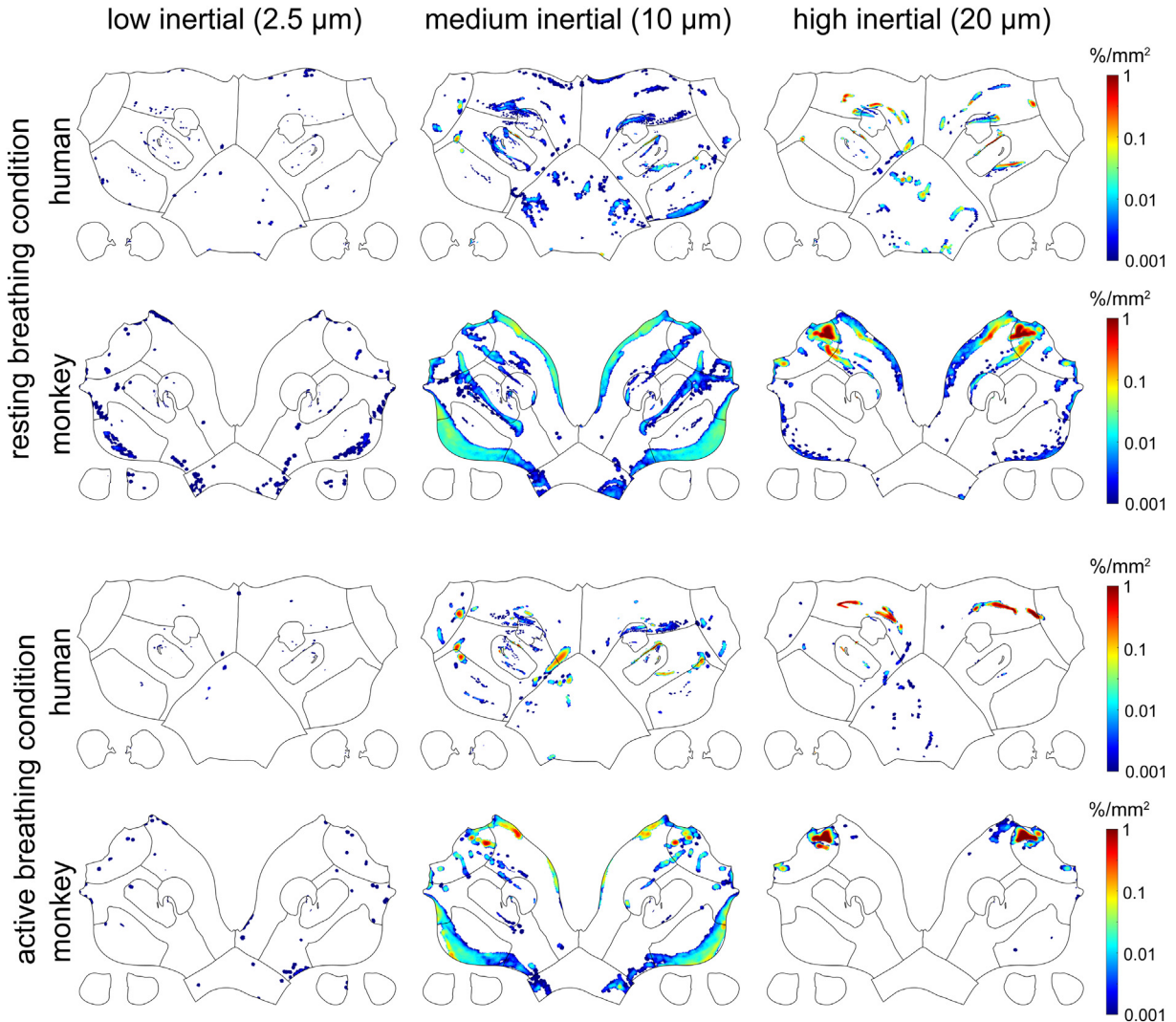


Fig. 6. Comparisons of particle intensity (PI) patterns between human and monkey cases under resting and active breathing conditions. Particle intensity contours of low inertial ($2.5\text{ }\mu\text{m}$), medium inertial ($10\text{ }\mu\text{m}$) and high inertial ($20\text{ }\mu\text{m}$) particles were plotted.

in resting and active conditions, respectively). However, in the human case, there is only one observable peak at $10\text{ }\mu\text{m}$ for the resting breathing condition, with the maximum DE value around 5 %. Another major difference can be observed in the posterior-vestibule region, presenting the opposite situation to the vestibule region. The S-shape profiles for the human case indicate the particles escaped from the vestibule region are mostly trapped in the posterior-vestibule region, whereas the DE profiles for the monkey case drop rapidly after reaching peaks at $16\text{ }\mu\text{m}$ and $11\text{ }\mu\text{m}$ for resting and active breathing conditions, respectively.

4. Discussion

Monkeys are frequently used to assess toxicological effects of environmental particles on human due to similarities in physiology and anatomy. As the front defender of the respiratory system, it is essential to compare particle depositions in the nasal cavities between monkey and human. This study conducted CFD simulations on a monkey nasal model and a human nasal model, and found the total nasal deposition efficiencies share similar characteristics between two species, as evidenced in Figs. 3 that all deposition curves can be normalized into a single correlation using stokes number. This also shows agreement with literature (Kelly et al., 2005; Lu Phuong et al., 2018), where normalized microparticle deposition curves were developed between monkey and human nasal models.

However, the slight geometrical difference between human and monkey nasal cavities makes it difficult to conduct region-specific cross-species hazards extrapolations. This study numerically predicted detailed microparticles deposition characteristics between monkey and human nasal walls using surface mapping method, as shown in Figs. 4–6. Coupled with regional deposition efficiency curves in Fig. 7, two major cross-species differences of regional deposition can be observed. Fig. 8 explains these differences by visualizing airflow streamlines from top and side views of human and monkey nasal cavities under active breathing conditions.

First, for high inertial particles, the vestibule region of the monkey nasal cavity serves as an efficient filter whereas the posterior-vestibule regions are dominant regions that capture deposited particles, escaping from the vestibule region. As seen from top views of Fig. 8, the monkey nostrils open more to the opposite sides of the face when compared to human. The angle between the inspiratory airflow and the posterior-vestibule mainstreams is roughly 60 degrees whereas it is roughly 30 degrees for the human case. Similar phenomena were observed in the literature of a human-monkey nasal airflow comparison study (Tian et al., 2022). This oblique-shaped nostril direction creates a sharp turn for the airflow in the vestibule region of the monkey, thus efficiently capturing high inertial particles. Another factor can be seen from the side view of the human nasal cavity (Fig. 8). The nasal valve, located at the posterior part of the vestibule, exhibits notched structures that alter the respiratory airflow patterns with a concave upper surface recess and prevent particles from depositing. This

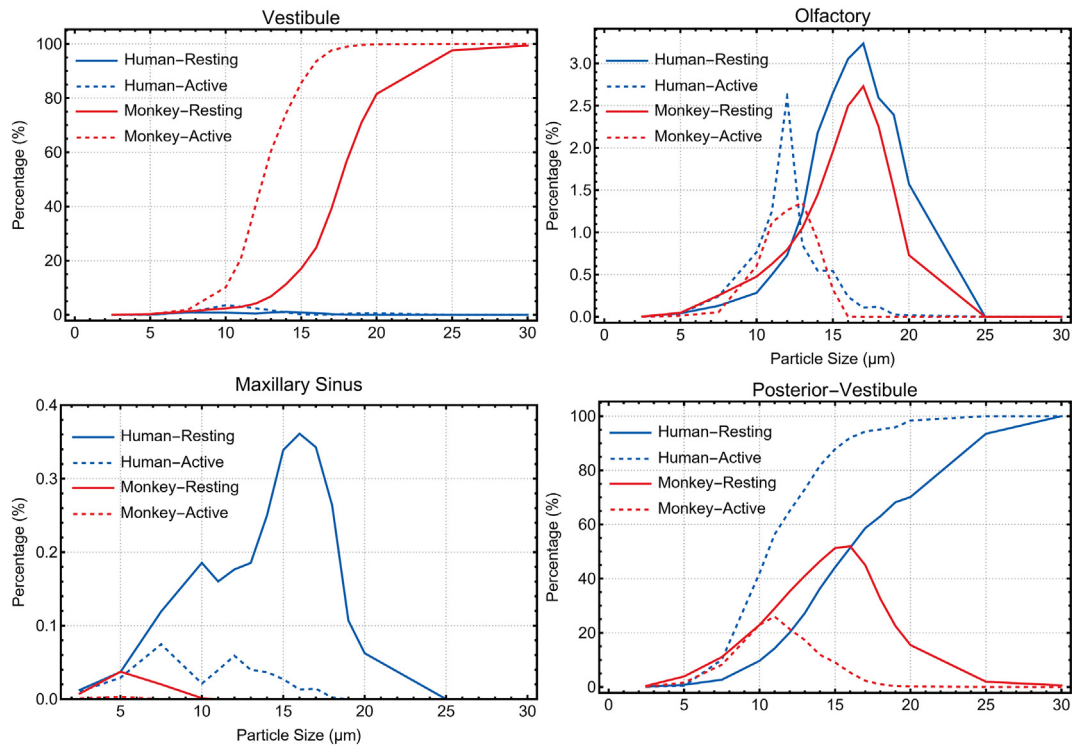


Fig. 7. Regional deposition curves against particle sizes on vestibule, olfactory, maxillary sinus and posterior-vestibule regions. Both human and monkey cases and both resting and active breathing conditions were plotted.

feature is consistent with literature (Tian et al., 2022; Ramprasad and Frank-Ito, 2016; Ma et al., 2020).

Second, medium inertial particles dominantly deposit on the floor of the monkey nasal cavity, but this is not observed in the human case. As seen from the side views of airflow streamlines in Fig. 8, the high-speed airflows

are located at different regions of human and monkey nasal cavities. For the monkey case, the high-speed airflow is dominantly concentrated around the nasal valve region, and significantly decelerates when escaping the vestibule, thus resulting in deposition on the floor of the nasal cavity. Whereas for the human case, the high-speed airflow is observed at the nasopharynx

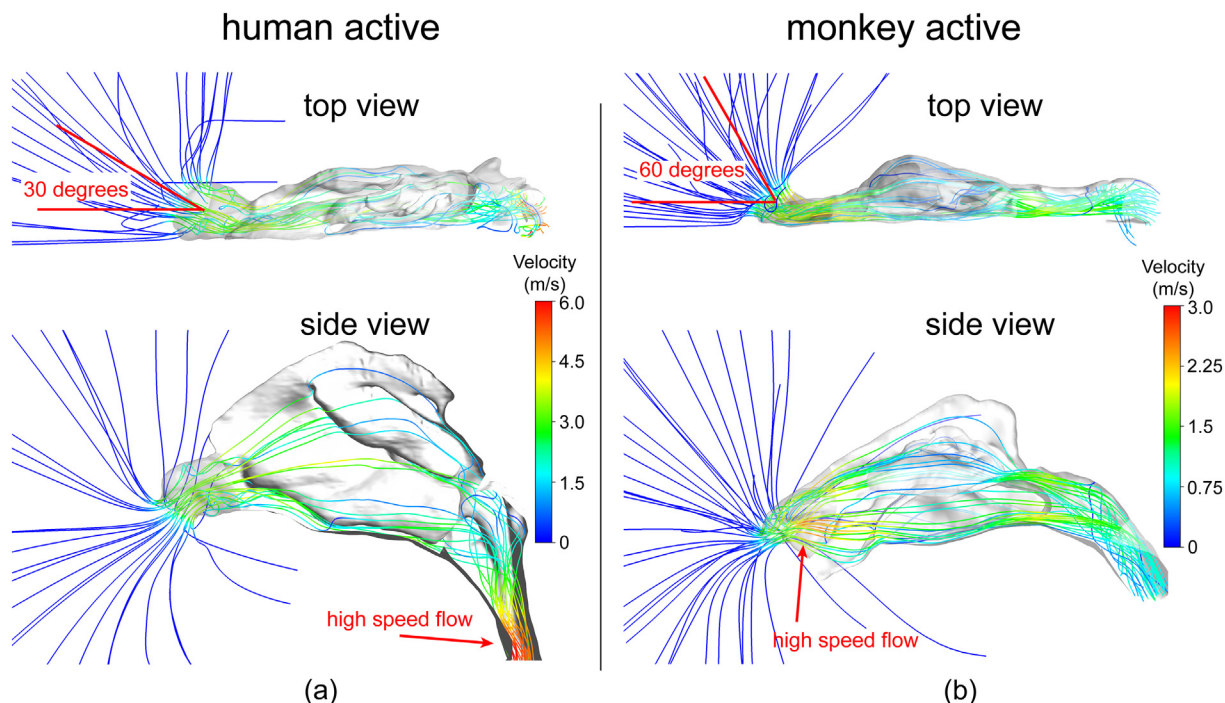


Fig. 8. Streamlines visualized to reveal different airflow features between (a) human and (b) monkey nasal cavities. Top and side views were plotted. The inflow mainstream directions and high-speed flow regions were indicated by arrows.

where airflow streams from two nasal chambers merge to one stream. Compared to the monkey case, the airflow around the nasal valve is much less accelerated and this is also observed in Lin et al. (Tian et al., 2022).

Besides observed variations in airflow patterns, the quantified localized particle deposition results (i.e., particle intensity, PI) was in conjunction with our novel surface mapping technique (Fig. 6) to allow accurate and efficient identification of deposition hot spots in these two species. This quantified information is expected to play an important role in calculating human's equivalent exposure concentration in targeted tissue, especially when site-specificity is important for inhalation toxicity. In addition, the regional deposition efficiency profiles of major nasal cavity regions (including vestibule, olfactory, maxillary sinus and posterior-vestibule regions) under resting and active inhalation conditions (Fig. 7) are expected to offer valuable insights for toxicological and other related professionals in adjusting exposure scenarios to achieve desired or equivalent regional deposition dose. For example, due to evidenced superior filtration effect for inertial particles in the monkey nasal cavity, particle sizes exceeding 20 μm are not recommended for conducting inhalation test in monkey surrogates. This is because most inhaled particles will be trapped and wasted in the vestibule regions, which are covered by less permeable squamous epithelium. In this way, the present numerical modelling efforts can best contribute towards refined human risk assessments for occupational and residential exposures by preventing or reducing the number of animal toxicity study attempts under unrealistic exposure scenarios.

5. Conclusion

This study numerically investigated in-depth microparticle transport and deposition characteristics on human and monkey (*Macaca fuscata*) nasal cavities that were reconstructed from CT-images. Deposition characteristics of 1–30 μm particles were investigated under resting and active breathing conditions. Similar trends were observed for total deposition efficiencies. A single correlation using Stokes Number was fitted for both species and both breathing conditions, which is convenient for monkey-human extrapolation. Regional deposition patterns were carefully compared using the surface mapping technique. Deposition patterns of low, medium and high inertial particles, classified based on their total deposition efficiencies, were further analyzed in the 3D view and the mapped 2D view, which allows locating particle depositions on specific nasal regions. According to the particle intensity contours and regional deposition profiles, the major differences were observed at the vestibule and the floor of the nasal cavity, where higher deposition intensities of medium and high inertial particles were shown in the monkey case than the human case. Comparisons of airflow streamlines indicated that the cross-species variations of microparticle deposition patterns are mainly contributed by two factors. First, the more oblique directions of monkey nostrils result in a sharper airflow turn in the vestibule region. Second, the monkey's relatively narrower nasal valves lead to higher impaction of medium and high inertial particles on the nasal cavity floor. This paper offers a numerical solution to conduct comparative particle deposition analysis on cross-species nasal cavity subjects. Research findings in this study contribute to an improved cross-species toxicological extrapolation between human and monkey nasal cavities.

Although the present numerical approach and findings have removed some long-standing inhalation exposure data extrapolation obstacles between monkey and human species, some assumptions and modelling restrictions are recognized as the research limitation. In more detail, the effect of inter-subject variability on the transport and deposition characteristics of environmental microparticles may slightly alter the current localized and regional deposition data. This limitation can be addressed by including additional nasal cavity subjects from both species. In addition, ambient particles often cover a wide spectrum of size distribution. These particles exhibit strong regional variability, reflecting local/regional differences in emission sources, transport, and ambient chemical/physical processes. Therefore, future numerical inhalation exposure tests should consider realistic particle size distribution, which can certainly improve the credibility and significance of the results.

CRediT authorship contribution statement

Yidan Shang: Conceptualization, Methodology, Formal analysis, Data curation, Visualization and Writing- Original draft preparation.

Jingliang Dong: Conceptualization, Validation, Writing- Reviewing and Editing, Funding acquisition.

Fajiang He: Resources.

Kiao Inthavong: Software and Visualization.

Lin Tian: Investigation and Writing- Reviewing and Editing.

Jiyuan Tu: Conceptualization, Supervision and Project administration.

Data availability

Data will be made available on request.

Declaration of competing interest

The authors declare that they have no known competing financial interests or personal relationships that could have appeared to influence the work reported in this paper.

Acknowledgement

The financial supports provided by the Program for Professor of Special Appointment (Eastern Scholar) at Shanghai Institutions of Higher Learning (Project ID: 0920000016), the Australian Research Council (Grant No. DE210101549) and the National Natural Science Foundation of China (Grant No. 81800096) are gratefully acknowledged.

References

- Albuquerque-Silva, I., et al., 2014. Particle deposition in a child respiratory tract model: *in vivo* regional deposition of fine and ultrafine aerosols in baboons. *PLoS One* 9 (4), e95456.
- Attems, J., Walker, L., Jellinger, K.A., 2014. Olfactory bulb involvement in neurodegenerative diseases. *Acta Neuropathol.* 127 (4), 459–475.
- Bide, R., Armour, S., Yee, E., 2000. Allometric respiration/body mass data for animals to be used for estimates of inhalation toxicity to young adult humans. *J. Appl. Toxicol.* 20 (4), 273–290.
- Corley, R.A., et al., 2012. Comparative computational modeling of airflows and vapor dosimetry in the respiratory tracts of rat, monkey, and human. *Toxicol. Sci.* 128 (2), 500–516.
- Corley, R.A., et al., 2021. New approach methodology for assessing inhalation risks of a contact respiratory cytotoxin: computational fluid dynamics-based aerosol dosimetry modeling for cross-species and *in vitro* comparisons. *Toxicol. Sci.* 182 (2), 243–259.
- Dabisch, P., et al., 2017. Quantification of regional aerosol deposition patterns as a function of aerodynamic particle size in rhesus macaques using PET/CT imaging. *Inhal. Toxicol.* 29 (11), 506–515.
- DeSesso, J., 1993. The relevance to humans of animal models for inhalation studies of cancer in the nose and upper airways. *Qual. Assur. (San Diego, Calif.)* 2 (3), 213–231.
- Dong, J., et al., 2017. Numerical comparison of nasal aerosol administration systems for efficient nose-to-brain drug delivery. *Pharm. Res.* 35 (1), 5.
- Dong, J., Tian, L., Ahmadi, G., 2019. Numerical assessment of respiratory airway exposure risks to diesel exhaust particles. *Exp. Comput. Multiphase Flow* 1 (1), 51–59.
- Dong, J., et al., 2021. Numerical analysis of nanoparticle transport and deposition in a cynomolgus monkey nasal passage. *Int. J. Numer. Methods Biomed. Eng.* 37 (2), e3414.
- Dong, J., et al., 2021. Transport and deposition of ultrafine particles in the upper tracheobronchial tree: a comparative study between approximate and realistic respiratory tract models. *Comput. Methods Biomed. Eng.* 24 (10), 1125–1135.
- Doty, R.L., 2008. The olfactory vector hypothesis of neurodegenerative disease: is it viable? *Ann. Neurol.* 63 (1), 7–15.
- EPA, U., 2018. Strategic Plan to Promote the Development and Implementation of Alternative Test Methods Within the TSCA Program. Environmental Protection Agency, United States.
- Garcia, G.J., Schroeter, J.D., Kimbell, J.S., 2015. Olfactory deposition of inhaled nanoparticles in humans. *Inhal. Toxicol.* 27 (8), 394–403.
- Geisler, T.S., et al., 2019. Simulation of microparticle inhalation in rhesus monkey airways. *Phys. Rev. Fluids* 4 (8), 083101.
- Gross, E., et al., 1987. Morphometric analysis of the primate nasal cavity. *Toxicologist* 7, 193.
- Health-Effects-Institute, 2020. State of Global Air 2020.
- Illum, L., 2004. Is nose-to-brain transport of drugs in man a reality? *J. Pharm. Pharmacol.* 56 (1), 3–17.
- Inthavong, K., 2020. From indoor exposure to inhaled particle deposition: a multiphase journey of inhaled particles. *Exp. Comput. Multiphase flow* 2 (2), 59–78.
- Inthavong, K., Shang, Y., Tu, J., 2014. Surface mapping for visualization of wall stresses during inhalation in a human nasal cavity. *Respir. Physiol. Neurobiol.* 190, 54–61.

- Kelly, J.T., Asgharian, B., Wong, B.A., 2005. Inertial particle deposition in a monkey nasal mold compared with that in human nasal replicas. *Inhal. Toxicol.* 17 (14), 823–830.
- Kesavan, J.S., Alstadt, V.J., Laube, B.L., 2020. Aerosol deposition in 3D models of the upper airways and trachea of rhesus macaques. *Aerosol Sci. Technol.* 54 (8), 983–991.
- Kimbell, J., 2006. Nasal dosimetry of inhaled gases and particles: where do inhaled agents go in the nose? *Toxicol. Pathol.* 34 (3), 270–273.
- KUPRI, 2022. Digital Morphology Museum.
- Lu Phuong, N., et al., 2018. Particle and inhalation exposure in human and monkey computational airway models. *Inhal. Toxicol.* 30 (11–12), 416–428.
- Ma, J., et al., 2018. Air conditioning analysis among human nasal passages with anterior anatomical variations. *Med. Eng. Phys.* 57, 19–28.
- Ma, J., et al., 2020. A combined computational and experimental study on nanoparticle transport and partitioning in the human trachea and upper bronchial airways. *Aerosol Air Qual. Res.* 20 (11), 2404–2418.
- MacLoughlin, R.J., et al., 2016. Optimization and dose estimation of aerosol delivery to non-human primates. *J. Aerosol Med. Pulm. Drug Deliv.* 29 (3), 281–287.
- Mo, J.-H., 2019. Association of particulate matter with ENT diseases. *Clin. Exp. Otorhinolaryngol.* 12 (3), 237.
- Morsi, S., Alexander, A., 1972. An investigation of particle trajectories in two-phase flow systems. *J. Fluid Mech.* 55 (2), 193–208.
- Phillips, K.A., et al., 2014. Why primate models matter. *Am. J. Primatol.* 76 (9), 801–827.
- Ramprasad, V.H., Frank-Ito, D.O., 2016. A computational analysis of nasal vestibule morphologic variabilities on nasal function. *J. Biomech.* 49 (3), 450–457.
- Schroeter, J.D., et al., 2008. Application of physiological computational fluid dynamics models to predict interspecies nasal dosimetry of inhaled acrolein. *Inhal. Toxicol.* 20 (3), 227–243.
- Schroeter, J.D., Garcia, G.J., Kimbell, J.S., 2011. Effects of surface smoothness on inertial particle deposition in human nasal models. *J. Aerosol Sci.* 42 (1), 52–63.
- Schroeter, J.D., et al., 2013. Computational fluid dynamics simulations of inhaled nano-and microparticle deposition in the rhesus monkey nasal passages. *Inhal. Toxicol.* 25 (12), 691–701.
- Schroeter, J.D., et al., 2014. Effects of endogenous formaldehyde in nasal tissues on inhaled formaldehyde dosimetry predictions in the rat, monkey, and human nasal passages. *Toxicol. Sci.* 138 (2), 412–424.
- Shang, Y., Inthavong, K., 2019. Numerical assessment of ambient inhaled micron particle deposition in a human nasal cavity. *Exp. Comput. Multiphase Flow* 1 (2), 109–115.
- Shang, Y., Inthavong, K., Tu, J., 2015. Detailed micro-particle deposition patterns in the human nasal cavity influenced by the breathing zone. *Comput. Fluids* 114, 141–150.
- Shang, Y., et al., 2021. Quantification of long-term accumulation of inhaled ultrafine particles via human olfactory-brain pathway due to environmental emissions—a pilot study. *NanoImpact* 22, 100322.
- Shi, H., Kleinstreuer, C., Zhang, Z., 2007. Modeling of inertial particle transport and deposition in human nasal cavities with wall roughness. *J. Aerosol Sci.* 38 (4), 398–419.
- Siu, J., et al., 2021. Nasal air conditioning following total inferior turbinectomy compared to inferior turbinoplasty—a computational fluid dynamics study. *Clin. Biomech.* 81, 105237.
- Subbaraman, N., 2021. The US is boosting funding for research monkeys in the wake of COVID. *Nature* 595 (7869), 633–634.
- Tian, L., et al., 2022. Detailed comparison of anatomy and airflow dynamics in human and cynomolgus monkey nasal cavity. *Comput. Biol. Med.* 141, 105150.
- Vahaji, S., et al., 2022. Interspecies comparison of heat and mass transfer characteristics in monkey and human nasal cavities. *Comput. Biol. Med.* 147, 105676.
- World-Health-Organisation, 2021. Ambient (outdoor) air pollution - key facts. Available from: [https://www.who.int/news-room/fact-sheets/detail/ambient-\(outdoor\)-air-quality-and-health](https://www.who.int/news-room/fact-sheets/detail/ambient-(outdoor)-air-quality-and-health).
- World-Health-Organisation, 2021. Household air pollution and health - key facts. Available from: <https://www.who.int/news-room/fact-sheets/detail/household-air-pollution-and-health>.